Research Article

Nano Research
2023, 16(3): 4004–4012

ISSN 1998-0124 CN 11-5974/O4
https://doi.org/10.1007/s12274-022-5226-1

A bioactive nanocomposite sponge for simultaneous hemostasis and antimicrobial therapy

Jiani Lei[1,§], Shanshan Li[1,§], Shuang Liu[1], Qingyuan Wu[1], Bolong Xu[1], Zhijun Huang[2], Nier Wu[3], Xiaolu Xiong[3], Huiyu Liu[1] (✉), and Dongsheng Zhou[3] (✉)

[1] *Beijing Advanced Innovation Center for Soft Matter Science and Engineering, State Key Laboratory of Organic–Inorganic Composites, Bionanomaterials & Translational Engineering Laboratory, Beijing Key Laboratory of Bioprocess, Beijing Laboratory of Biomedical Materials, Beijing University of Chemical Technology, Beijing 100029, China*

[2] *Beijing National Laboratory of Molecular Sciences, Key Laboratory of Green Printing, Institute of Chemistry, Chinese Academy of Sciences, Beijing 100190, China*

[3] *State Key Laboratory of Pathogen and Biosecurity, Beijing Institute of Microbiology and Epidemiology, Beijing 100071, China*

[§] *Jiani Lei and Shanshan Li contributed equally to this work.*

Received: 15 August 2022 / **Revised:** 10 October 2022 / **Accepted:** 19 October 2022

ABSTRACT

Uncontrollable bleeding and bacterial infections are the major reasons for the high mortality of post-traumatic. In this study, a composite hemostatic chitosan sponge CaO_2@SiO_2/CS was prepared by combining a novel core–shell inorganic nano hemostatic CaO_2@SiO_2 nanoparticles with carboxylated chitosan, which presents a multi-layered structure with a rough and hydrophilic surface for rapid absorption of blood. When the CaO_2@SiO_2 nanoparticles in the CaO_2@SiO_2/CS come into contact with blood, the silanol group on its surface and the released H_2O_2 and Ca^{2+} can recruit and activate platelets, while generating fibrin clots and activating the endo-exogenous coagulation cascade reaction to achieve rapid clotting. The H_2O_2 released from CaO_2@SiO_2 shows the antimicrobial capacity and stimulates the production of tissue factors by endothelial cells. Meanwhile, the silica coating reduces the cytotoxicity of bare CaO_2, thus reducing the risk of secondary bleeding at the site of vascular injury. CaO_2@SiO_2/CS (48 s) showed a 1.83- and 2.52-fold reduction in hemostasis time compared to commercial gelfoam and CS in a femoral artery hemorrhage model. This study illustrates the hemostatic mechanism of CaO_2@SiO_2 and provides a reference for the development of clinical biomedical inorganic hemostatic materials.

KEYWORDS

calcium peroxide, coagulation mechanism, composite sponge, hemostasis, antibacterial

1 Introduction

Uncontrolled hemorrhage after a traumatic accident causes approximately more than 33% of pre-hospital deaths [1]. Significant blood loss can lead to serious complications such as hypothermia, acidosis, multiple organ failure, shock, and an increased risk of fatal infections [2, 3]. Traditionally, gauze and mechanical hemostatic agents have been used to plug the wound with pressure to stop bleeding but may associate with ischemic complications [4]. Drugs with active coagulation properties such as collagen and thrombin are often used in combination with kaolin, zeolite, chitosan, and other materials as hemostatic agents [3, 5–7]. It has been reported that the introduction of inorganic materials into hemostatic materials can substantially improve hemostasis efficiency [8, 9]. However, the severe foreign body reaction induced by inorganic materials is still a serious problem. For example, the first generation of zeolite-based QuikClot used by the USA military in 2002 caused severe thermal tissue damage at the wound sites [10]. The physicochemical properties of inorganic materials are crucial for hemostasis and post-healing. Combat gauze, a typical inorganic gauze based on inorganic zeolite and kaolin shows an excellent hemostatic effect, which is mainly attributed to the high specific surface area and porosity of the silica [11, 12]. Although the use of silica has reduced the biological toxicity of inorganic materials, the secondary bleeding and bacterial infections accompanying the hemostasis process remain a challenge in the clinic. It is significant to develop new multifunctional inorganic materials-based hemostatic agents with high biosafety, long-lasting effects, and antibacterial properties for emergency trauma and subsequent treatment.

Nanometer metal oxides, such as Fe_2O_3 [13, 14], ZnO [15, 16], CuO [17], and TiO_2 [18], not only exhibit good hemostatic effects but also show antibacterial and tissue repair activities, due to their unique physicochemical properties and biological effects [19]. However, the potential toxicity of metal ions such as Cu^{2+} and Zn^{2+} cannot be ignored. Ca^{2+} is one of the essential components of the human body, which can act as a second messenger participating in most of the life activities of the body, showing higher biosafety and lower systemic toxicity than other nano-hemostatic agents. More importantly, Ca^{2+} can act as the coagulation factor IV to drive the initiation and development of the coagulation process [20, 21]. Thus, the efficiency of Ca^{2+}-enhanced hemostasis is an important

Address correspondence to Huiyu Liu, liuhy@mail.buct.edu.cn; Dongsheng Zhou, zhouds@bmi.ac.cn

reason why researchers continue to develop calcium-based hemostatic agents. However, current Ca^{2+}-based hemostatic agents have limited hemostatic properties and have not demonstrated antimicrobial effects. Therefore, it is important to develop multifunctional and safe calcium-based compound hemostatic agents. Ca^{2+} can be produced by the reaction of CaO_2 with H_2O, which is accompanied by the production of hydrogen peroxide (H_2O_2). H_2O_2 as a small molecule plays a vital role in activating platelet and promoting the production of tissue factor (TF) by endothelial cells in the hemostatic process [22, 23]. Therefore, CaO_2 has great potential in hemostatic and antibacterial applications. But the reaction is rapid and violent, and the instantaneous production of large amounts of H_2O_2 will inevitably cause secondary damage to the wound. The surface coating of the porous structure can slow down the diffusion rate of H_2O thus controlling the chemical reaction rate [24]. This strategy is expected to solve the disadvantages of CaO_2, bringing a new choice for developing next-generation multifunctional hemostatic agents.

Here, a composite hemostatic chitosan (CS) sponge named $CaO_2@SiO_2$/CS with excellent coagulation property and a long-lasting antibacterial effect was synthesized (Scheme 1). Surface silanol groups together with Ca^{2+} and H_2O_2 released by $CaO_2@SiO_2$ nanoparticles (NPs) can rapidly aggregate and activate platelets, promote fibrinogen production, and accelerate the activation of extrinsic and intrinsic pathways achieving rapid clotting. In addition, the long-lasting release of H_2O_2 can cause the expression of TF by endothelial cells, which could reduce the risk of secondary bleeding. The combination of carboxylated chitosan and $CaO_2@SiO_2$ NPs reduced the risk of thrombosis caused by the massive exposure of nanoparticles to blood vessels. Compared to commercial gelfoam sponge or CS, the $CaO_2@SiO_2$/CS provides faster and more effective hemostasis and antibacterial capabilities. Therefore, we believe the $CaO_2@SiO_2$/CS sponge can provide a new idea for the development of novel multifunctional antibacterial hemostatic agents.

2 Experimental

2.1 Preparation of CaO_2 NPs

The synthesis of CaO_2 was performed according to a reported method [25]. Typically, $CaCl_2$ (1 g) and polyvinyl pyrrolidone (PVP, 3 g) were dissolved in 150 mL ethanol under ultrasound.

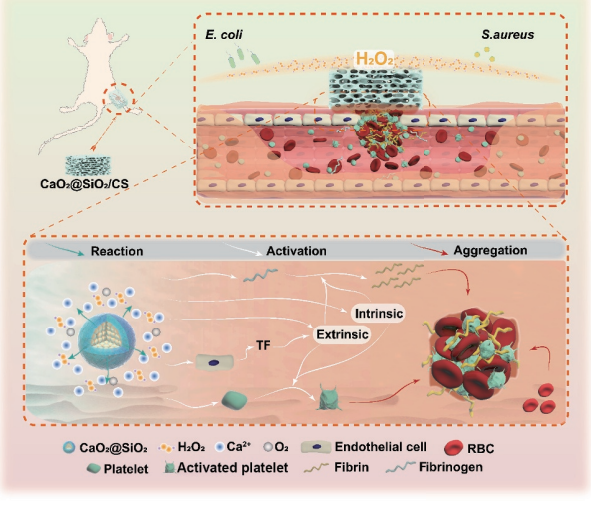

Scheme 1 Schematic illustration of hemostatic and antibacterial actions of $CaO_2@SiO_2$/CS. Extrinsic pathway and intrinsic pathway are the two classic pathways of secondary hemostasis.

Then 10 mL of NH_4OH (1 M) was added under stirring at 300 rpm. 6 mL H_2O_2 (1 M) was added at a rate of 0.04 mL·min^{-1} and stirred for 2 h. The CaO_2 NPs were then formed and washed three times with ethanol. The CaO_2 NPs were collected in 2 mL of ethanol for further use.

2.2 Preparation of $CaO_2@SiO_2$ and $CaO@SiO_2$ NPs

1 mL of the obtained CaO_2 NPs solution was diluted with 15 mL ethanol in a round bottom flask under ultrasound. 1 mL of 25%–28% (w/w) NH_4OH was added. Different volumes of tetraethylorthosilicate (TEOS) (0.1, 0.2, 0.4, and 0.8 mL) dissolved in 7.2 mL ethanol were then added dropwise to the flasks, respectively. After being reacted for 12 h at 30 °C, the products were collected by centrifugation at 9,000 rpm, and washed thrice with ethanol, dried at 60 °C. The calcium contents of CaO_2, $CaO_2@SiO_2$-1, $CaO_2@SiO_2$-2, $CaO_2@SiO_2$-3, and $CaO_2@SiO_2$ with different thicknesses of SiO_2 were determined by inductively coupled plasma-mass spectrometry (ICP-MS), where 1, 2, and 3, represent the volumes of TEOS 0.1, 0.2, and 0.4 mL, respectively added in the above reaction systems. $CaO_2@SiO_2$ is the abbreviation of $CaO_2@SiO_2$ with the added volume of TEOS 0.8 mL for the main text.

$CaO@SiO_2$ was obtained by calcining $CaO_2@SiO_2$ at 540 °C for 2 h under an oxygen atmosphere. The transmission electron microscope (TEM) image of $CaO@SiO_2$ is shown in Fig. S8(a) in the Electronic Supplementary Material (ESM), the surface potential of $CaO@SiO_2$ was −15.8 mV (Fig. S8(b) in the ESM). The X-ray diffraction (XRD) pattern was consistent with amorphous silicon (Fig. S8(c) in the ESM). Further experiments showed that no H_2O_2 or O_2 was released from $CaO@SiO_2$ (Figs. S8(d) and S8(e) in the ESM), but there had no significant difference in Ca^{2+} release between $CaO@SiO_2$ (19.87 μg·mL^{-1}) and $CaO_2@SiO_2$ (21.44 μg·mL^{-1}) within 30 min reaction (Fig. S8(f) in the ESM).

2.3 Synthesis of $CaO_2@SiO_2$/CS

5 mL of carboxylated chitosan solution with 2% (w/w) mass fraction (sodium hydroxide solution in the solvent of pH 8.5) was added to a beaker. 0.1 mL 1% (w/w) of glutaraldehyde and 1 mL 5% (w/w) of D-mannitol were added and stirred at 800 rpm for 10 min, and then rested for 2 h. After the liquid solution changed to a gel state, $CaO_2@SiO_2$ NPs (mass ratios of 0.2, 0.4, 0.6, and 0.8 to carboxylated chitosan) were quickly and uniformly added to the gel, respectively, followed by freeze-drying for 24 h to obtain the $CaO_2@SiO_2$/CS sponges with different mass ratios of $CaO_2@SiO_2$ to carboxylated chitosan: 0.2:1, 0.4:1, 0.6:1, and 0.8:1. $CaO_2@SiO_2$/CS is the abbreviation of $CaO_2@SiO_2$/CS with the ratio of 0.6:1 for the main text.

2.4 Evaluation of H_2O_2 production

The H_2O_2 release curve was tested with the neocuproine reagents. The concentration of neocuproine and copper sulfate was 10 mM. The standard curve of H_2O_2 was first measured in a 96-well plate. 50 μL neocuproine and 50 μL copper sulfate solutions were mixed, and 90 μL ultrapure water was added. After mixing, H_2O_2 with different concentrations (6.25, 5, 3.75, 1.875, and 0 mM) were added. The absorbance at 450 nm was tested to obtain the standard curve of H_2O_2 (Fig. S4 in the ESM). The calcium contents of CaO_2, $CaO_2@SiO_2$-1, $CaO_2@SiO_2$-2, $CaO_2@SiO_2$-3, and $CaO_2@SiO_2$ were 0.3552, 0.3172, 0.2145, 0.1206, and 0.1023 mg·mg^{-1} respectively measured by ICP-MS. To ensure consistent calcium ion concentrations, the $CaO_2@SiO_2$ at a concentration of 10 mg·mL^{-1} was used as a standard to configure the rest of the material. The absorbance was then measured at 450 nm during 0–6 h. The concentration of the released H_2O_2 was

calculated through the standard curve measured before.

2.5 Measurement of O_2 generation

Materials were mixed with 5 mL of deoxy ultrapure water, respectively, and the O_2 generation was detected by multi-parameter analyzer (JPSJ-606L, Leici China). To ensure the consistency of calcium ion concentrations, the mass of materials was settled as follows: 10 mg of CaO_2@SiO_2, 2.88 mg of CaO_2, 3.23 mg of CaO_2@SiO_2-1, 4.75 mg of CaO_2@SiO_2-2, and 8.48 mg of CaO_2@SiO_2-3.

2.6 *In vitro* cell cytotoxicity test

Murine fibroblast (NIH-3T3) cell line was purchased from Beijing Vital River Laboratory Animal Technology Co., Ltd. For *in vitro* cytotoxicity test, NIH-3T3 cells were seeded into 96 well plates with a density of 1×10^4 cells per well. After 24 h of incubation, cells were incubated with CaO_2, CaO_2@SiO_2-1, CaO_2@SiO_2-2, CaO_2@SiO_2-3, and CaO_2@SiO_2, respectively. To ensure consistent calcium ion concentrations, the CaO_2@SiO_2 at different concentrations of (0, 0.0625, 0.125, 0.25, 0.50, and 1.00 mg·mL^{-1}) were used as a standard to configure the other materials at the same calcium ion concentrations. After incubation for another 24 h, the 3-(4,5-dimethylthiazol-2-yl)-2,5-diphenyltetrazolium bromide (MTT) assay was used to determine the cytotoxicity according to a standard protocol.

2.7 Live/dead assay

NIH-3T3 cells (5×10^4 per well) were seeded in confocal dishes for 12 h, 0.5 mg·mL^{-1} of CaO_2@SiO_2 and 0.14 mg·mL^{-1} of CaO_2 dissolved in Dulbecco's modified Eagle medium (DMEM) culture medium were added, respectively. After 12 h of incubation, the cells were stained with calcine acetoxymethylester (AM) and propidium iodide (PI) (KeyGEN Biotech, Nanjing, China) following the protocol and observed by a Leica SP5 confocal laser scanning microscope (CLSM).

2.8 Hemolysis assay *in vitro*

50 μL red blood cells were mixed with different concentrations of materials (CaO_2@SiO_2 or CaO_2). After incubation for 1 h at 37 °C, the mixtures were centrifugated at 3,000 rpm for 5 min. The absorption of the supernatants at 540 nm was tested on a BioTek Powerwave XS fluorescence microplate reader. Ultrapure water and phosphate buffered solution (PBS) were settled as positive and negative controls, respectively. The hemolysis ratio was calculated by Eq. (1)

$$\text{Hemolysis}\ (\%) = (A_s - A_p)/(A_w - A_p) \times 100\% \quad (1)$$

where A_s, A_p, and A_w are the absorptions of the sample suspension, PBS, and ultrapure water at 540 nm, respectively.

2.9 Blood clotting time (BCT) assay

Fresh anticoagulated blood was obtained by mixing male Sprague–Dawley (SD) rat blood with 3.8% sodium citrate. 2 mg of samples (CaO_2, CaO_2@SiO_2, CaO@SiO_2, and kaolin) and fresh anticoagulated blood were preheated at 37 °C for 5 min before the experiment. The preheated samples were added into a 5 mL glass tube, respectively. Nothing was added for the control group. Then, 500 μL of fresh anticoagulant blood, mixed with 100 μL of $CaCl_2$ (25 mM) solutions were added to the samples. The glass tubes were tilted every 15 s to observe the status of blood and recorded the BCTs of different groups.

2.10 The interaction between blood and material

1 μL of H_2O_2 (25 mM), 1 mg of CaO_2@SiO_2, and CaO@SiO_2 were placed on the slides respectively. Subsequently, 20 μL of fresh anticoagulated blood and 4 μL of calcium chloride solution (25 mM) were added dropwise to coverslips and adhered to the slides. After incubation for 15 min at 37 °C, the sealed slides were observed and captured with a microscope.

2.11 Prothrombin time (PT) and activated partial thromboplastin time (APTT) measurements

The clinical standard coagulation tests, PT and APTT, were performed by using a semiautomatic coagulation analyzer (XL 1000e, Zhongchi). Platelet-poor plasma (PPP) was obtained by centrifugation of anticoagulated blood at 2,500*g* for 15 min. 400 μL of PPP was incubated with 2 mg of CaO_2, CaO_2@SiO_2, CaO@SiO_2, and kaolin respectively at 37 °C for 10 min. PT and APTT were then measured. The negative control was PPP without other substances.

2.12 Enzyme linked immunosorbent assay (ELISA) for TF assay

The human umbilical vein endothelial cells (HUVECs, 2×10^7 per well) were seeded in plates for 24 h, then 0.50 mg·mL^{-1} of CaO_2@SiO_2, 0.50 mg·mL^{-1} of CaO@SiO_2, and 0.14 mg·mL^{-1} of CaO_2 dissolved in DMEM culture medium were added respectively. After 8 h, different groups of supernatants were collected and the amount of TF was measured by ELISA (Cloud-Clone Corp., item No. SEA524Hu). The standard curve was tested and calculated in Fig. S10 in the ESM.

2.13 The interaction of platelet with materials

Platelet-rich plasma (PRP) was obtained by centrifugation of anticoagulated blood at 150 g for 5 min and diluted with PPP to a concentration of 2×10^7 cells·mL^{-1}. 10 μL of different materials (H_2O_2 (25 mM), $CaCl_2$ (25 mM), CaO_2 (2.88 mg·mL^{-1}), CaO_2@SiO_2, CaO@SiO_2, and kaolin (10 mg·mL^{-1})) were incubated with 190 μL of PRP respectively at 37 °C for 20 min. Then, the samples were fixed with 2.5% glutaraldehyde for 2 h. The samples were dehydrated in a series of ethanol solutions (30%, 50%, 70%, 90%, and 100% v/v) and observed by scanning electron microscope (SEM).

2.14 Alexa Fluor™ 488-labeled fibrin clots assay

Alexa Fluor™ 488-labeled fibrin clots measurement was conducted by the addition of bovine fibrinogen and Alexa Fluor™ 488-labeled fibrinogen into different groups: (I) $CaCl_2$ + thrombin; (II) thrombin; (III) CaO_2@SiO_2; and (IV) CaO_2@SiO_2 + thrombin. After being incubated at 37 °C for 20 min, the production of fibrin was observed by CLSM. The final concentrations of materials in this part were: 2.5 mg·mL^{-1} of bovine fibrinogen, 1 U·mL^{-1} of thrombin, 0.125 mg·mL^{-1} of Alexa Fluor™ 488-fibrinogen, 1.25 mM of $CaCl_2$, and 0.5 mg·mL^{-1} of CaO_2@SiO_2.

2.15 Whole blood clotting assay

Preparation materials: commercial gelfoam sponge, CS sponge, and CaO_2@SiO_2/CS sponges with different mass ratios of CaO_2@SiO_2 to carboxylated chitosan: 0.2:1, 0.4:1, 0.6:1, and 0.8:1 were cut into blocks of 8 mm × 8 mm × 2.5 mm in 6-well plate respectively and preheated at 37 °C for 30 min. 50 μL of the citrated whole blood was slowly dispensed and dripped onto the surface of sponges and the samples were followed by the addition of $CaCl_2$ (10 μL, 25 mM) at 37 °C with 80 rpm on the shaker. Next, at 0, 30, 60, 120, 180, and 240 s time points, 5 mL of distilled water was carefully added to the 6-well plate of each sponge at 37 °C and shook at 80 rpm for 1 min. Then, the absorption of supernatants for each group was measured at 540 nm. Finally, the

blood clotting index (BCI) of the samples in each group was calculated from Eq. (2)

$$BCI = A/A_0 \times 100\% \quad (2)$$

The absorbance of citrated whole blood (50 μL) with $CaCl_2$ (10 μL, 25 mM) was used as the control group. A_0 is the absorbance of the control group at 0 s and A is the absorbance of the samples.

The interaction of the whole blood with each material was observed by SEM. The sponges (gelfoam, CS, and CaO_2@SiO_2/CS sponges) were immersed in citrated blood for 15 min. Then, the sponges of the samples were washed with PBS (pH 7.4) to remove the non-adherent blood cells. After being fixed with 2.5% glutaraldehyde tissue fixator for 2 h, the sponge samples were dehydrated in a series of ethanol solutions (30%, 50%, 70%, 90%, and 100% v/v) and observed by SEM.

2.16 *In vitro* antibacterial assay

Bacteria culture: two bacterial strains, namely *Escherichia coil* ATCC 29522 and *Staphylococcus aureus* ATCC 29213, were used to evaluate the antibacterial effect. CaO_2 (0.14 mg·mL^{-1}), CaO_2@SiO_2 (0.50 mg·mL^{-1}), and CaO@SiO_2 (0.50 mg·mL^{-1}) were incubated with Luria–Bertani (LB) medium for 1, 4, and 7 days. At each incubation time point, *E. coli* or *S. aureus* was added and incubated at 37 °C for 12 h. The mixed solutions were then coated on plates and incubated at 37 °C for 12 h. The numbers of colonies were counted. Gelfoam, CS, and CaO_2@SiO_2/CS sponges with different mass ratios of CaO_2@SiO_2 to carboxylated chitosan: 0.2:1, 0.4:1, 0.6:1, and 0.8:1 were cut into Ø8 mm × 2.5 mm circles and placed in solid media coated with *E. coli* or *S. aureus* respectively and incubated at 37 °C for 12 h. The sizes of the inhibition circle were measured. In the above experiments, the concentration of *E. coli* or *S. aureus* was 10^6 CFU·mL^{-1}.

2.17 *In vivo* antibacterial and wound-healing evaluation

BALB/c male mice (6 weeks, 15–18 g) were purchased from Vital River Laboratories (Beijing, China). All animal experiments were approved (IACUC–DWZX–2022–032) and followed the guidance of the care and use of laboratory animals. A wound approximately 6 mm in diameter was established on the dorsum of each mouse. Then, the infected wound model was constructed after injecting 10 μL suspension of *S. aureus* with 1×10^9 CFU·mL^{-1} into the wound areas. After 24 h, the mice were randomly divided into four groups: PBS, gelfoam, CS, and CaO_2@SiO_2/CS (Ø6 mm × 2.5 mm). Photographs and wound areas of the wound in each group were taken on days 0, 1, 3, 5, and 7. The body weight of mice was also measured. The mice were sacrificed after 7 days and the granulation tissues over the wound bed were harvested and fixed in 4% paraformaldehyde overnight, followed by dehydration and embedded in paraffin for pathological histology analysis.

2.18 *In vivo* femoral artery cut experiment

Sprague-Dawley (SD) rats (male, weight 250–300 g) were anesthetized with chloral hydrate. Then, 2 cm of the femoral artery and vein were exposed after the soft thigh tissues were transected with a scalpel. Uncontrolled hemorrhage was created by completely severing the femoral artery and vein. To quantify the hemorrhage volume, the blood was absorbed using weighed gauze pieces. After free bleeding for 10 s, gelfoam, CS, and CaO_2@SiO_2/CS (each sponge weighing about 1,200 mg) were applied over the location of the injury. Manual compression was required to stop the bleeding. The control group was treated with standard gauze. The material was gently removed every 10 s to observe hemostasis, the time of hemostasis was recorded, and the liquid and clotted inguinal blood and hemostatic agents were removed and weighed.

3 Results and discussion

3.1 Preparation and characterization of CaO_2@SiO_2 NPs

CaO_2@SiO_2 NPs were fabricated following the process in Fig. 1(a). Briefly, CaO_2 NPs with an average particle size of about 75 nm were first prepared by chemical reduction of Ca^{2+} in the presence of H_2O_2 and PVP in an alkaline aqueous solution (Fig. 1(b)) [25]. The amorphous silica layer was then coated onto CaO_2 NPs through the hydrolysis of tetraethyl orthosilicate with the addition of ammonia. The thin $Ca(OH)_2$ layer on CaO_2 NPs provided the reactive sites for the generation of the SiO_2. The TEM image of the prepared CaO_2@SiO_2 NPs showed a uniform spherical shape with a size of about 157 nm (Fig. 1(c)). The high-resolution TEM (HR-TEM) image demonstrated the ordered lattice fringes of CaO_2@SiO_2 with the interplanar spacing of 0.293 and 0.242 nm (Fig. 1(d)), which corresponded to the (002) and (110) facets of CaO_2, respectively [25]. The powder XRD (PXRD) pattern (Fig. 1(e)) of the crystallinity of CaO_2@SiO_2 was consistent with that of standard powder CaO_2 (standards card number 03-0865) and SiO_2 (standards card number 13-0026). The Fourier transform infrared spectroscopy (FTIR) spectra were further used to detect the successful coating of the silica shell. As shown in Fig. S1 in the ESM, the peaks at 1,490, 1,087, and 453 cm^{-1} were assigned to O–Ca–O, Si–O–Si, and Si–OH respectively, suggesting the existence of SiO_2 [26, 27]. After coating of SiO_2, the surface potentials changed from +4.15 to −14.27 mV, which could attribute to the presence of Si–OH on the surface of CaO_2@SiO_2 NPs (Fig. 1(f)). Element mapping (Fig. 1(h)) and energy-dispersive spectrometry (EDS) analysis of CaO_2@SiO_2 NPs proved the presence of Ca, Si, O, and N elements (Fig. S2 in the ESM). The porosity of CaO_2@SiO_2 was also reflected by the nitrogen adsorption profiles (Fig. 1(g)), and the pore size of CaO_2@SiO_2 was about 1.6 nm, which was beneficial to the postponed release of H_2O_2.

The thickness of the SiO_2 shell in CaO_2@SiO_2 NPs had a direct effect on the release rate of H_2O_2 and Ca^{2+} and the biosafety of CaO_2@SiO_2 NPs. Samples with various thicknesses of SiO_2 shell were prepared by changing the amount of TEOS. The SiO_2 shell thickness of the CaO_2@SiO_2 samples increased with the increase of TEOS volume (Fig. S3 in the ESM). The average sizes of CaO_2@SiO_2-1, CaO_2@SiO_2-2, and CaO_2@SiO_2-3 were 103, 121, and 133 nm respectively.

3.2 Sustained release and biosafety of CaO_2@SiO_2 NPs

Schematic of H_2O_2, O_2, and Ca^{2+} release from CaO_2@SiO_2-x NPs is illustrated in Fig. 2(a). The release curves of H_2O_2 and O_2 from CaO_2@SiO_2-1, CaO_2@SiO_2-2, CaO_2@SiO_2-3, and CaO_2@SiO_2 were determined. As shown in Figs. 2(b) and 2(c), the release rates of H_2O_2 and O_2 decreased as the SiO_2 shell thickness increased during 6 h of incubation. Naked CaO_2, CaO_2@SiO_2-1, and CaO_2@SiO_2-2 released H_2O_2 and O_2 rapidly and reached the maximum within 1 h (Figs. S5(a) and S5(b) in the ESM), indicating their uncontrollable release property. By contrast, CaO_2@SiO_2 became slow, but the release curve still showed an upward trend at the 6-h time point. The release rates of Ca^{2+} from CaO_2@SiO_2 and naked CaO_2 were 0.257 and 0.686 μg·mL^{-1}·min^{-1} respectively during the first 1 h (Figs. S6(a) and S6(b) in the ESM). The morphology changes of particles were further observed by TEM. As shown in Fig. 2(d), the structure collapses and disintegrates within 1 h for naked CaO_2. For CaO_2@SiO_2, some CaO_2 still existed in the shell after 12 h reaction. After 120 h reaction, only the SiO_2 shell existed. These results proved that the coating of SiO_2 slows the reaction rate of CaO_2 and on the other hand avoided the cytotoxicity of burst H_2O_2 for normal cells.

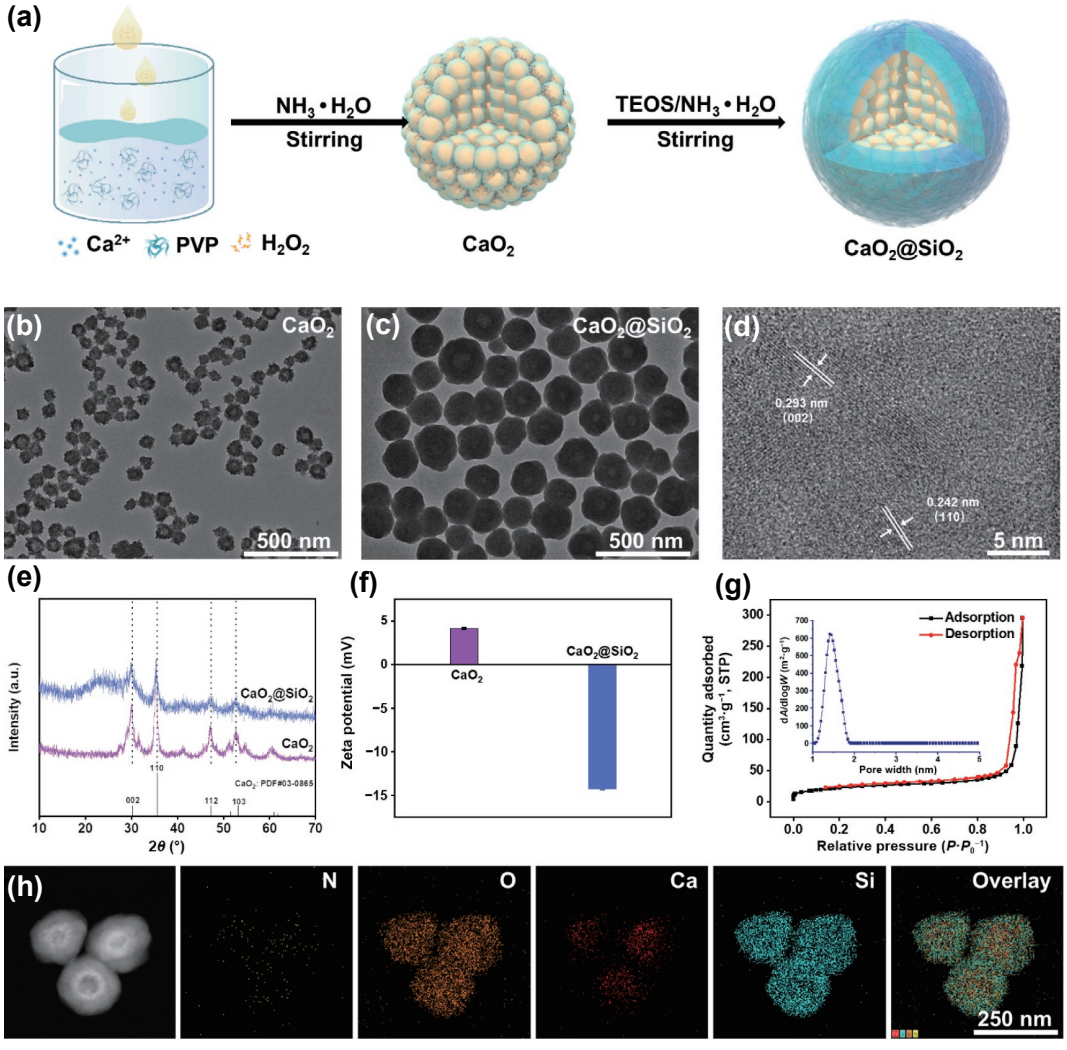

Figure 1 Synthesis and characterization of CaO_2@SiO_2. (a) Schematic illustration of the synthesis of CaO_2@SiO_2. TEM images of (b) CaO_2 and (c) CaO_2@SiO_2. (d) HR-TEM image of CaO_2@SiO_2. (e) XRD patterns of CaO_2 and CaO_2@SiO_2. (f) Zeta potential of CaO_2 and CaO_2@SiO_2. (g) Nitrogen adsorption and desorption isotherms of CaO_2@SiO_2, inset is the pore size distribution plot. (h) Scanning TEM (STEM) image of CaO_2@SiO_2 and the corresponding element mapping.

Mouse embryo-derived fibroblast NIH-3T3 was used to verify the biocompatibility of CaO_2, CaO_2@SiO_2-1,2,3, and CaO_2@SiO_2. As shown in Fig. 2(e), more than 90% of NIH-3T3 cells survived for CaO_2@SiO_2 at the concentration of 0.50 mg·mL^{-1}. The cytotoxicity for other groups gradually increased as the SiO_2 shell thickness decreased. The results from CLSM images (Fig. S7 in the ESM) also suggested the relatively good biosafety of CaO_2@SiO_2 NPs after co-culturing with NIH-3T3 cells for 12 h. The hemolysis rates of CaO_2@SiO_2 NPs and CaO_2 NPs were further evaluated which were less than 3% and 5% (Figs. 2(f) and 2(g)). Considering the biosafety, CaO_2@SiO_2 NPs were chosen as the hemostatic material for subsequent experiments.

3.3 *In vitro* hemostatic efficiency of CaO_2@SiO_2 NPs and mechanism

The clotting performances of CaO_2 NPs and CaO_2@SiO_2 NPs were evaluated by determining BCT, which was a basic method for characterizing a hemostatic agent. Blood alone was set as a negative control (control) and blood containing kaolin was set as a positive control (kaolin). As shown in Fig. 3(a), the BCTs of CaO_2 and CaO_2@SiO_2 groups were significantly lower than those of control and kaolin groups, suggesting the better clotting performance of CaO_2 NPs and CaO_2@SiO_2 NPs. The H_2O_2 and Ca^{2+} released from CaO_2 NPs and CaO_2@SiO_2 NPs would play critical roles in coagulation. It has been reported that Ca^{2+} can activate thrombin, which initiates the coagulation process and promotes hemostasis [20, 21]. To further investigate the effect of H_2O_2 on the coagulation process, another control material CaO@SiO_2 NP was prepared, which could not produce H_2O_2. The basic characterizations of CaO@SiO_2 NPs were presented in Fig. S8 in the ESM. The BCT (90 s) of CaO@SiO_2 was significantly higher than that (35 s) of CaO_2@SiO_2, suggesting that H_2O_2 produced by CaO_2@SiO_2 promoted hemostasis. When H_2O_2 was exposed to blood, the catalase enzyme in the blood rapidly catalyzed the production of O_2, and the produced O_2 created a gas–liquid barrier that assisted in facilitating the hemostatic process. As shown in Fig. S9 in the ESM, gas–liquid barriers were clearly seen in both H_2O_2 and CaO_2@SiO_2 groups.

To gain insight into the mechanism of hemostasis, the clinical standard coagulation tests were performed to determine APTT and PT, which are usually used to assess intrinsic and extrinsic pathways, respectively. As shown in Figs. 3(b) and 3(c), the APTTs and PTs of CaO_2, CaO_2@SiO_2, and CaO@SiO_2 groups were shorter than that of the control group, suggesting the positive effect of these nanoparticles on both intrinsic and extrinsic pathways for hemostasis. The APTTs (Fig. 3(b)) of the CaO_2 and CaO_2@SiO_2 groups were even lower than that of the kaolin group. It should be noted that the APTT of the CaO_2@SiO_2 group was higher than that of the CaO_2 group, suggesting that CaO_2 activated the intrinsic pathway. By contrast, the PT of the CaO_2@SiO_2 group was significantly lower than that of the CaO_2 group, suggesting that the silica shell activated the extrinsic pathway. The

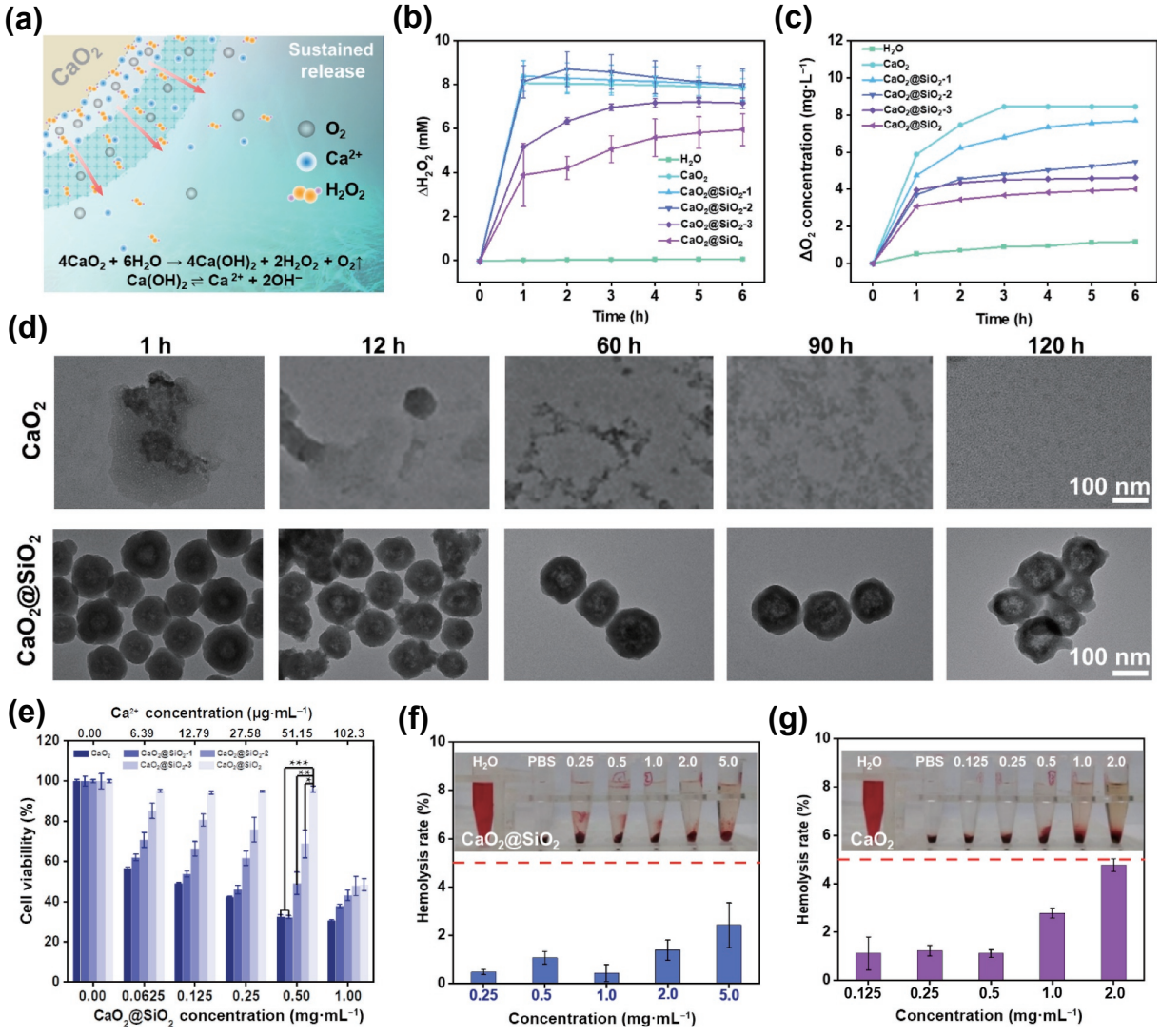

Figure 2 Sustained-release characterization and cytotoxicity assay of $CaO_2@SiO_2$ and CaO_2 NPs. (a) Schematic demonstration of H_2O_2 and O_2 release by $CaO_2@SiO_2$. (b) Determination of H_2O_2 contents released by CaO_2, $CaO_2@SiO_2$-*x* (*x* = 1, 2, and 3, representing different amounts of TEOS: 0.1, 0.2, and 0.4 mL), and $CaO_2@SiO_2$ (prepared with the amount of TEOS: 0.8 mL) in H_2O. (c) Determination of O_2 contents released by CaO_2, $CaO_2@SiO_2$-*x*, and $CaO_2@SiO_2$ in H_2O. (d) TEM images of CaO_2 and $CaO_2@SiO_2$ in H_2O at 37 °C within 120 h. (e) Cell viabilities of NIH-3T3 cells after incubation with CaO_2, $CaO_2@SiO_2$-*x*, or $CaO_2@SiO_2$ at different Ca^{2+} concentrations (0.00, 6.39, 12.79, 27.58, 51.15, and 102.30 μg·mL^{-1}). Hemolysis rates of (f) $CaO_2@SiO_2$ and (g) CaO_2 at different concentrations. The calcium concentrations in all the particles are consistent with that of $CaO_2@SiO_2$. Not significant (ns): $p > 0.05$, $^*p < 0.05$, $^{**}p < 0.01$, and $^{***}p < 0.001$.

silanol groups on the surface of the silica shell could catch the positively charged amino acids in blood coagulation factor XII, thus activating the extrinsic pathway [28]. In addition, the PT (Fig. 3(c)) of the $CaO_2@SiO_2$ group was lower than that of the $CaO@SiO_2$ group, suggesting that the release of H_2O_2 could also accelerate the extrinsic coagulation process. It has been reported that H_2O_2 can stimulate the production of TF, which activates platelets and triggers the extrinsic pathway to promote coagulation [23, 29]. To further verify the effect of H_2O_2 on the extrinsic pathway, ELISA was used to detect the amount of TF produced by HUVEC cells induced by different materials. As shown in Fig. S10(b) in the ESM, the TF amount in the $CaO_2@SiO_2$ group was 2.53-fold higher than that in the control group, and 2.86-fold higher than that in the $CaO@SiO_2$ group, indicating that H_2O_2 could induce TF overexpression in HUVEC cells. In addition, the much lower TF expression in the CaO_2 group might be caused by the severe toxicity of naked CaO_2 to HUVEC cells (Fig. S7 in the ESM).

When a blood vessel is damaged, platelets are rapidly activated, aggregated, and adhered to the damaged area, which then triggers a coagulation cascade for rapid hemostasis [30]. SEM was used to virtually observe the morphological changes of platelets after different treatments (Fig. 3(d)). The fresh platelets group (control) and PBS-treated group showed a smooth, spherical, and ellipsoidal surface and were evenly dispersed. Platelets treated with CaO_2 NPs or $CaO_2@SiO_2$ NPs piled up into clusters with irregular morphology and pseudopods protruding from the surface, suggesting the activated state of platelets. Platelets treated with $CaO@SiO_2$ NPs or kaolin exhibited only accumulated aggregation, and only a small number of platelets were activated. To further investigate the mechanism of activation of platelets by CaO_2 NPs and $CaO_2@SiO_2$ NPs, the platelets were treated with H_2O_2 or $CaCl_2$ and the results showed that H_2O_2 induced the activation of platelets, while $CaCl_2$ mainly promoted the aggregation of platelets.

During blood coagulation, thrombin converts soluble fibrinogen into an insoluble fibrin network structure, which is essential for blood clot stability [31]. As a promoter of coagulation, Ca^{2+} is involved in promoting the binding of thrombin and fibrinogen. To observe the action of $CaO_2@SiO_2$ on the transformation of fibrinogen, Alexa Fluor™ 488 was used to label the formed fibrin network structure. As shown in Fig. 3(e), group I ($CaCl_2$ + thrombin) exhibited a distinct interwoven fibrin network structure, whereas group IV ($CaO_2@SiO_2$ + thrombin)

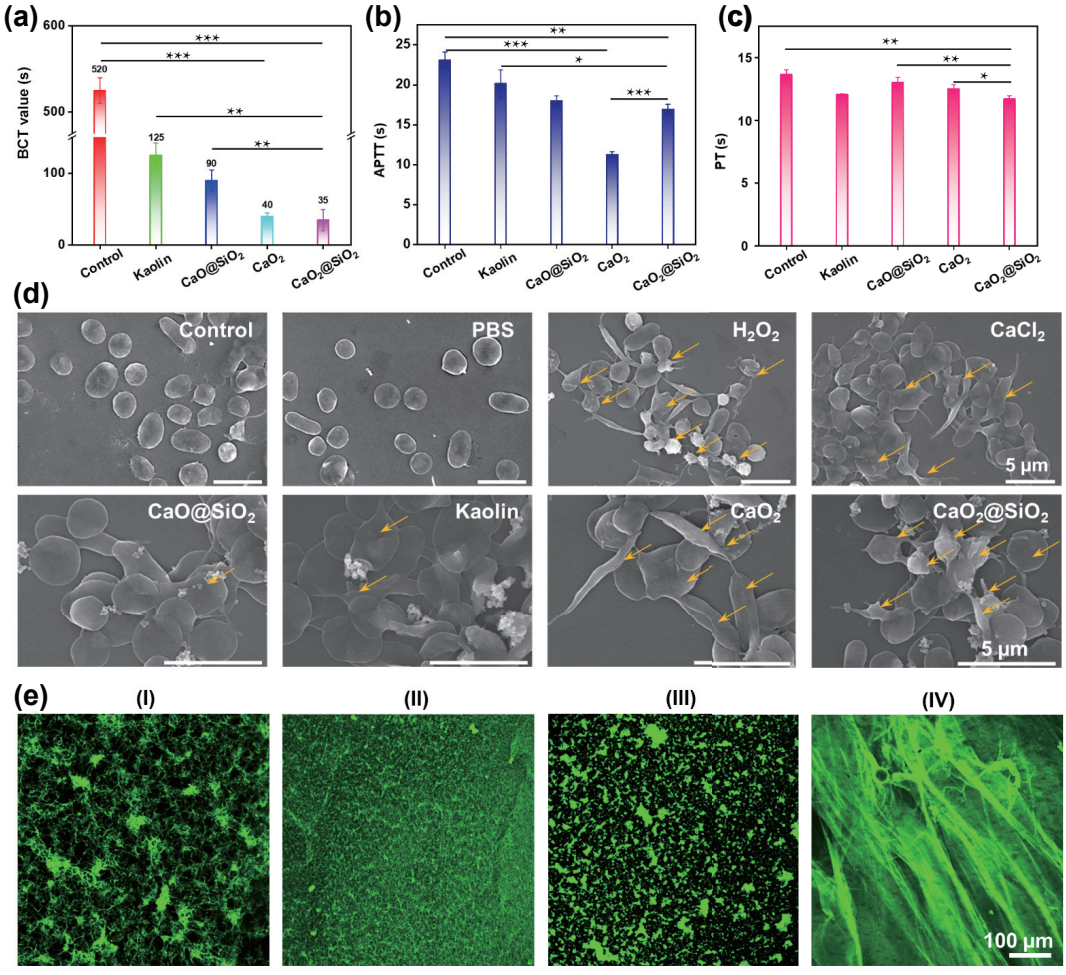

Figure 3 *In vitro* hemostatic mechanism of CaO_2@SiO_2 NPs. (a) BCT values of control, kaolin, CaO@SiO_2, CaO_2, and CaO_2@SiO_2. Changes of (b) APTT and (c) PT for PBS, kaolin, CaO@SiO_2, CaO_2, and CaO_2@SiO_2. (d) SEM images of platelet cells treated with PBS, H_2O_2, $CaCl_2$, CaO@SiO_2, kaolin, CaO_2 (0.14 mg·mL^{-1}), and CaO_2@SiO_2 (0.50 mg·mL^{-1}). (e) CLSM images of fibrin network in different groups. (Fibrinogen incubated with: (I) $CaCl_2$ + thrombin; (II) thrombin; (III) CaO_2@SiO_2; and (IV) CaO_2@SiO_2 + thrombin). ns: $p > 0.05$, $^*p < 0.05$, $^{**}p < 0.01$, and $^{***}p < 0.001$.

showed a larger and denser network structure, suggesting CaO_2@SiO_2 has a better promotion effect than Ca^{2+} alone on the connection of fibrin and thrombin. In addition, the formation rate of the fibrin network in the CaO_2@SiO_2 group was much faster than that in the $CaCl_2$ group (Fig. S11 in the ESM). These phenomena might correlate to the adsorption of fibrin and fibrinogen on the silica layer [32, 33].

3.4 Antibacterial property of CaO_2@SiO_2 NPs

Bacterial infection of wounds after traumatic hemorrhage has emerged as a non-negligible problem in the process of hemostasis and seriously affects the rate of wound healing. The antibacterial capability of CaO_2@SiO_2 was investigated *in vitro*. Firstly, CaO_2 NPs or CaO_2@SiO_2 NPs at 1, 4, and 7 days were co-incubated with *E. coli* or *S. aureus*. Both CaO_2 NPs and CaO_2@SiO_2 NPs showed excellent and long-term antibacterial effects, suggesting the coating of the SiO_2 shell did not influence the antimicrobial effect of CaO_2 NPs (Fig. S12 in the ESM).

3.5 *In vitro* hemostatic and antibacterial properties of CaO_2@SiO_2/CS sponges

Encouraged by the outstanding hemostatic and excellent antibacterial effects of CaO_2@SiO_2, we combined carboxylated chitosan and CaO_2@SiO_2 NPs to develop a composite chitosan sponge—CaO_2@SiO_2/CS, which was prepared by regulation the mass ratios of CaO_2@SiO_2 to carboxylated chitosan (0.2:1, 0.4:1, 0.6:1, and 0.8:1). CaO_2@SiO_2/CS and CS were characterized by SEM. As shown in Fig. 4(a) and Fig. S13(a) in the ESM, CaO_2@SiO_2 NPs were uniformly distributed on the spongy surface, and the sponge surface became progressively rough as the ratios of CaO_2@SiO_2 to carboxylated chitosan increased.

The coagulation properties of CaO_2@SiO_2/CS were assessed by visually observing the adhesion of blood cells onto the surface of CaO_2@SiO_2/CS and measuring the BCI. As shown in Fig. 4(a) and Fig. S13(a) in the ESM, CaO_2@SiO_2/CS showed a progressive increase in the number of adherent blood cells compared to gelfoam and CS. The smaller the BCI value, the better the coagulation ability of the sponge. The BCI values of CaO_2@SiO_2/CS varied along with the increase of the ratio of CaO_2@SiO_2 to carboxylated chitosan (Fig. S13(b) in the ESM). Over the initial 30 s, the BCI values at the mass ratios of 0.6:1 and 0.8:1 were far lower than those at other ratios. Moreover, the BCI value of CaO_2@SiO_2/CS (0.6:1) was more consistently maintained over time compared to CaO_2@SiO_2/CS (0.8:1), suggesting that the whole blood was almost completely clotted in CaO_2@SiO_2/CS (0.6:1) within 30 s. In particular, CaO_2@SiO_2/CS has a better clotting efficiency than commercial gauze and gelfoam (Fig. 4(b)). It might be attributed to the excellent hydrophilicity of CaO_2@SiO_2/CS, in which the water droplet was completely absorbed within 40 ms (Fig. 4(c) and Fig. S13(c) in the ESM). The antibacterial effects were further tested by measuring the inhibition zones of different groups. As shown in Fig. 4(d) and Figs. S13(d) and S13(e) in the ESM, CS and gelfoam showed no antibacterial activity, and CaO_2@SiO_2/CS exhibited a significant inhibition effect on both *E. coli* and *S. aureus*, and the inhibition zones gradually increased with the increase of CaO_2@SiO_2 ratio.

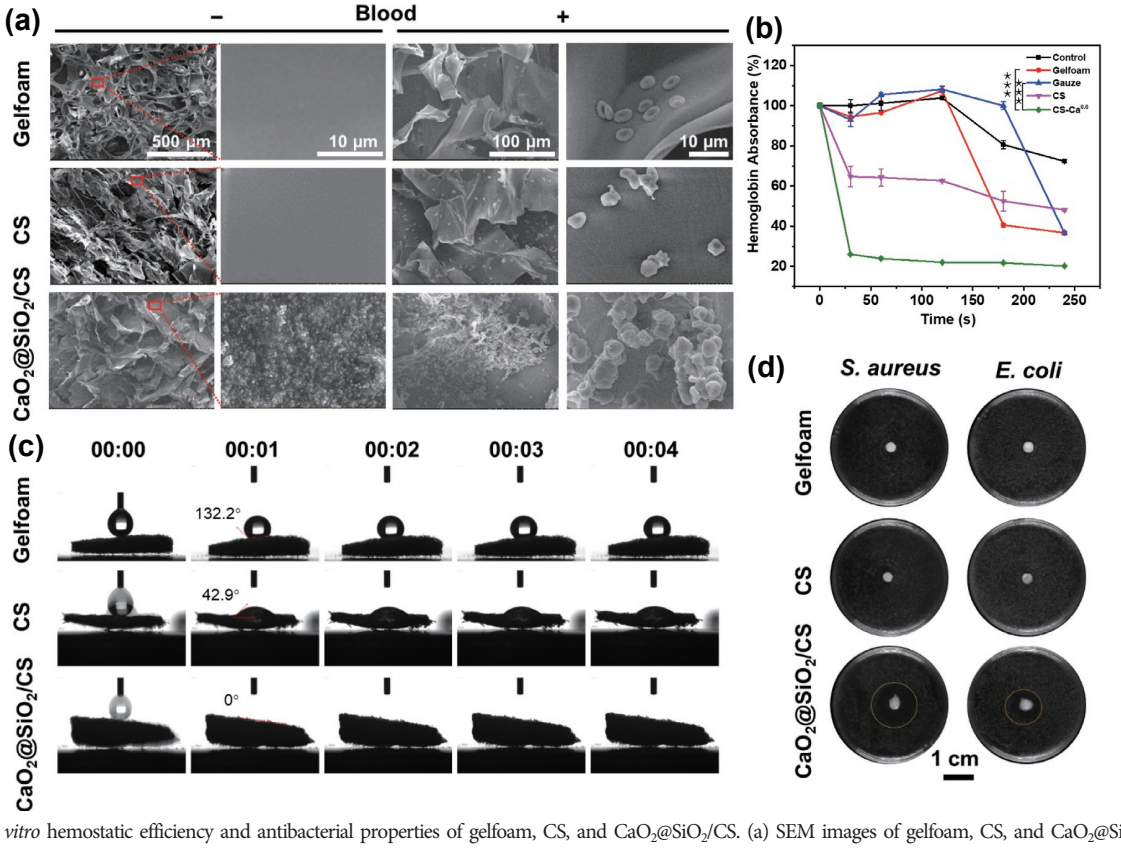

Figure 4 *In vitro* hemostatic efficiency and antibacterial properties of gelfoam, CS, and CaO_2@SiO_2/CS. (a) SEM images of gelfoam, CS, and CaO_2@SiO_2/CS (the mass ratio of the CaO_2@SiO_2 to carboxylated chitosan was 0.6:1) before and after co-incubation with whole blood for 15 min. (b) BCI values and (c) water contact angles of gelfoam, CS, and CaO_2@SiO_2/CS. (d) Representative photographs of *E. coli* and *S. aureus* plates of different hemostatic materials. ns: $p > 0.05$, $^{*}p < 0.05$, $^{**}p < 0.01$, and $^{***}p < 0.001$.

3.6 *In vivo* hemostatic and biosafety of CaO_2@SiO_2/CS sponge

Given the excellent hemostatic and antibacterial properties of CaO_2@SiO_2/CS described above, the *in vivo* hemostatic efficiency was further assessed by adopting the rat femoral artery injury model (Fig. 5(a)). CaO_2@SiO_2/CS had a hemostatic time of 48 ± 5 s and a blood loss of 106 ± 40 mg showing a much better hemostatic effect, compared to gelfoam (87.67 ± 15 s, 126 ± 12 mg) and CS (121 ± 20 s, 180 ± 36 mg) (Figs. 5(b) and 5(c)).

The biological toxicity of CaO_2@SiO_2/CS was further evaluated *in vivo*. The wound infection model was established by using *S. aureus* to infect cutaneous wounds in mice (Fig. S14(a) in the ESM). The traumas on days 0, 1, 3, 5, and 7 were photographed and the wound areas and bodyweights of mice after different treatments were measured. Results indicated that the wound areas of the CaO_2@SiO_2/CS group were 0.794 and 0.787 times lower than those of the control and gelfoam groups, respectively (Fig. S14(b) in the ESM). There was no obvious loss of body weight for all groups (Fig. S14(c) in the ESM). The wound tissues of mice were collected and subjected for hematoxylin and eosin (H&E) staining on 7 days post-treatment (Fig. S14(d) in the ESM), and no obvious abnormalities or lesions were observed. These results indicated that CaO_2@SiO_2/CS would be a promising hemostatic sponge.

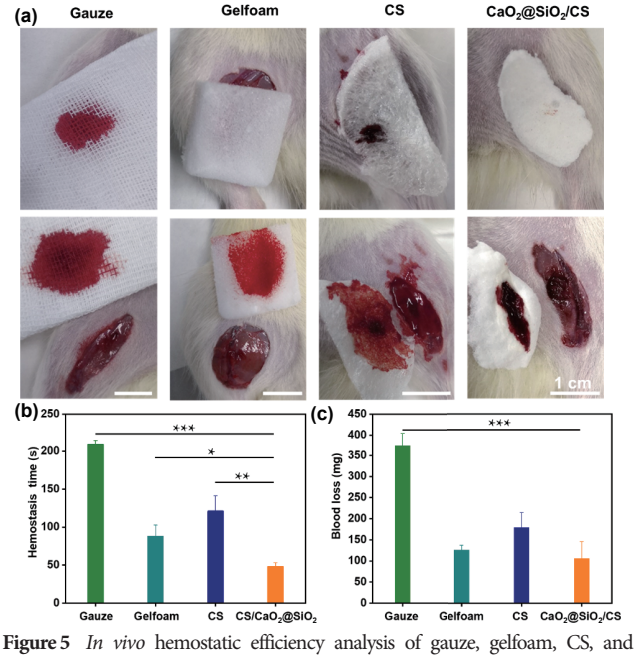

Figure 5 *In vivo* hemostatic efficiency analysis of gauze, gelfoam, CS, and CaO_2@SiO_2/CS. (a) The *in vivo* hemostatic experiment using the SD rat artery injury model, treated by gauze, gelfoam, CS, or CaO_2@SiO_2/CS. (b) Hemostatic time and (c) total blood loss for gauze, gelfoam, CS, or CaO_2@SiO_2/CS. ns: $p > 0.05$, $^{*}p < 0.05$, $^{**}p < 0.01$, and $^{***}p < 0.001$.

4 Conclusions

This is the first report of utilization of CaO_2 NPs coated with a silica shell for hemostatic and antibacterial therapies. The prepared CaO_2@SiO_2 NPs not only show low biological toxicity, but also have good hemostatic and antibacterial effects. CaO_2@SiO_2 NPs can activate intrinsic and extrinsic pathways, active platelets, accelerate fibrin production, and stimulate TF expression by releasing H_2O_2 and Ca^{2+}. The composite sponge CaO_2@SiO_2/CS prepared from CaO_2@SiO_2 NPs shows much better *in vitro* and *in vivo* hemostatic and antibacterial effects compared to CS and gelfoam. The method of using CaO_2@SiO_2 NPs as added active materials to improve the hemostatic and antibacterial effects of CS or other hemostatic agents is simple and universal. CaO_2@SiO_2/CS

would open a new view for the development of novel inorganic nano hemostatic agents.

Acknowledgements

This work was supported by the National Key Research and Development Program of China (No. 2021YFC2102900), the National Natural Science Foundation of China (Nos. U21A2085 and 22061130205), the Fundamental Research Funds for the Central Universities and Research Projects on Biomedical Transformation of China-Japan Friendship Hospital (No. XK2022-08), and the open Foundation of State Key Laboratory of Organic–Inorganic Composites, Beijing University of Chemical Technology (No. OIC-202201010).

Electronic Supplementary Material: Supplementary material (some additional experimental data being helpful to support the conclusions of this study) is available in the online version of this article at https://doi.org/10.1007/s12274-022-5226-1.

References

[1] Gruen, R. L.; Brohi, K.; Schreiber, M.; Balogh, Z. J.; Pitt, V.; Narayan, M.; Maier, R. V. Haemorrhage control in severely injured patients. *Lancet* **2012**, *380*, 1099–1108.

[2] Cannon, J. W. Hemorrhagic shock. *N. Engl. J. Med.* **2018**, *378*, 370–379.

[3] Hickman, D. A.; Pawlowski, C. L.; Sekhon, U. D. S.; Marks, J.; Gupta, A. S. Biomaterials and advanced technologies for hemostatic management of bleeding. *Adv. Mater.* **2018**, *30*, 1700859.

[4] Jamal, L.; Saini, A.; Quencer, K.; Altun, I.; Albadawi, H.; Khurana, A.; Naidu, S.; Patel, I.; Alzubaidi, S.; Oklu, R. Emerging approaches to pre-hospital hemorrhage control: A narrative review. *Ann. Transl. Med.* **2021**, *9*, 1192.

[5] Li, Z.; Milionis, A.; Zheng, Y.; Yee, M.; Codispoti, L.; Tan, F.; Poulikakos, D.; Yap, C. H. Superhydrophobic hemostatic nanofiber composites for fast clotting and minimal adhesion. *Nat. Commun.* **2019**, *10*, 5562.

[6] Zhong, Y. T.; Hu, H. Y.; Min, N. N.; Wei, Y. F.; Li, X. D.; Li, X. R. Application and outlook of topical hemostatic materials: A narrative review. *Ann. Transl. Med.* **2021**, *9*, 577.

[7] Wang, L. Y.; You, X. R.; Dai, C. L.; Tong, T.; Wu, J. Hemostatic nanotechnologies for external and internal hemorrhage management. *Biomater. Sci.* **2020**, *8*, 4396–4412.

[8] Yang, X.; Liu, W.; Li, N.; Wang, M. S.; Liang, B.; Ullah, I.; Luis Neve, A.; Feng, Y. K.; Chen, H.; Shi, C. C. Design and development of polysaccharide hemostatic materials and their hemostatic mechanism. *Biomater. Sci.* **2017**, *5*, 2357–2368.

[9] Pinkas, O.; Zilberman, M. Effect of hemostatic agents on properties of gelatin-alginate soft tissue adhesives. *J. Biomater. Sci. Polym. Ed.* **2014**, *25*, 555–573.

[10] Pourshahrestani, S.; Zeimaran, E.; Djordjevic, I.; Kadri, N. A.; Towler, M. R. Inorganic hemostats: The state-of-the-art and recent advances. *Mater. Sci. Eng. C* **2016**, *58*, 1255–1268.

[11] Ding, S.; Wei, X. H.; Yang, K.; Lin, S.; Tian, F.; Li, F. Ca-Ga double doping strategy to fabricate hemostatic mesoporous silica nanoparticles (MSN) with antibacterial activity. *Silicon* **2021**, *13*, 4033–4045.

[12] Chen, Z. H.; Han, L.; Liu, C. J.; Du, Y.; Hu, X.; Du, G.; Shan, C.; Yang, K.; Wang, C. L.; Li, M. G. et al. A rapid hemostatic sponge based on large, mesoporous silica nanoparticles and N-alkylated chitosan. *Nanoscale* **2018**, *10*, 20234–20245.

[13] Meddahi-Pellé, A.; Legrand, A.; Marcellan, A.; Louedec, L.; Letourneur, D.; Leibler, L. Organ repair, hemostasis, and *in vivo* bonding of medical devices by aqueous solutions of nanoparticles. *Angew. Chem., Int. Ed.* **2014**, *53*, 6369–6373.

[14] Li, Q.; Hu, E. L.; Yu, K.; Lu, M. X.; Xie, R. Q.; Lu, F.; Lu, B. T.; Bao, R.; Lan, G. Q. Magnetic field-mediated Janus particles with sustained driving capability for severe bleeding control in perforating and inflected wounds. *Bioact. Mater.* **2021**, *6*, 4625–4639.

[15] Tavakoli, S.; Kharaziha, M.; Nemati, S. Polydopamine coated ZnO rod-shaped nanoparticles with noticeable biocompatibility, hemostatic and antibacterial activity. *Nano-Struct. Nano-Objects* **2021**, *25*, 100639.

[16] Rao, K. M.; Suneetha, M.; Park, G. T.; Babu, A. G.; Han, S. S. Hemostatic, biocompatible, and antibacterial non-animal fungal mushroom-based carboxymethyl chitosan-ZnO nanocomposite for wound-healing applications. *Int. J. Biol. Macromol.* **2020**, *155*, 71–80.

[17] Venkataprasanna, K. S.; Prakash, J.; Vignesh, S.; Bharath, G.; Venkatesan, M.; Banat, F.; Sahabudeen, S.; Ramachandran, S.; Devanand Venkatasubbu, G. Fabrication of chitosan/PVA/GO/CuO patch for potential wound healing application. *Int. J. Biol. Macromol.* **2020**, *143*, 744–762.

[18] Hyde, G. K.; Stewart, S. M.; Scarel, G.; Parsons, G. N.; Shih, C. C.; Shih, C. M.; Lin, S. J.; Su, Y. Y.; Monteiro-Riviere, N. A.; Narayan, R. J. Atomic layer deposition of titanium dioxide on cellulose acetate for enhanced hemostasis. *Biotechnol. J.* **2011**, *6*, 213–223.

[19] Gaston, E.; Fraser, J. F.; Xu, Z. P.; Ta, H. T. Nano- and micro-materials in the treatment of internal bleeding and uncontrolled hemorrhage. *Nanomed. Nanotechnol. Biol. Med.* **2018**, *14*, 507–519.

[20] Singh, S.; Dodt, J.; Volkers, P.; Hethershaw, E.; Philippou, H.; Ivaskevicius, V.; Imhof, D.; Oldenburg, J.; Biswas, A. Structure functional insights into calcium binding during the activation of coagulation factor XIII A. *Sci. Rep.* **2019**, *9*, 11324.

[21] Palta, S.; Saroa, R.; Palta, A. Overview of the coagulation system. *Indian. J. Anaesth.* **2014**, *58*, 515–523.

[22] Pignatelli, P.; Pulcinelli, F. M.; Lenti, L.; Gazzaniga, P. P.; Violi, F. Hydrogen peroxide is involved in collagen-induced platelet activation. *Blood* **1998**, *91*, 484–490.

[23] Sen, C. K.; Roy, S. Redox signals in wound healing. *Biochim. Biophys. Acta Gen. Subj.* **2008**, *1780*, 1348–1361.

[24] Kong, L.; Chen, C. R.; Mou, F. Z.; Feng, Y. Z.; You, M.; Yin, Y. X.; Guan, J. G. Magnesium particles coated with mesoporous nanoshells as sustainable therapeutic-hydrogen suppliers to scavenge continuously generated hydroxyl radicals in long term. *Part. Part. Syst. Charact.* **2019**, *36*, 1800424.

[25] Shen, S.; Mamat, M.; Zhang, S. C.; Cao, J.; Hood, Z. D.; Figueroa-Cosme, L.; Xia, Y. N. Synthesis of CaO_2 nanocrystals and their spherical aggregates with uniform sizes for use as a biodegradable bacteriostatic agent. *Small* **2019**, *15*, 1902118.

[26] Liang, Y. J.; Ouyang, J.; Wang, H. Y.; Wang, W. L.; Chui, P. F.; Sun, K. N. Synthesis and characterization of core–shell structured SiO_2@YVO_4: Yb^{3+}, Er^{3+} microspheres. *Appl. Surf. Sci.* **2012**, *258*, 3689–3694.

[27] Rastinfard, A.; Nazarpak, M. H.; Moztarzadeh, F. Controlled chemical synthesis of CaO_2 particles coated with polyethylene glycol: Characterization of crystallite size and oxygen release kinetics. *RSC Adv.* **2018**, *8*, 91–101.

[28] Fröhlich, E. Action of nanoparticles on platelet activation and plasmatic coagulation. *Curr. Med. Chem.* **2016**, *23*, 408–430.

[29] Zhu, G.; Wang, Q.; Lu, S.; Niu, Y. Hydrogen peroxide: A potential wound therapeutic target? *Med. Princ. Pract.* **2017**, *26*, 301–308.

[30] Hou, Y.; Carrim, N.; Wang, Y. M.; Gallant, R. C.; Marshall, A.; Ni, H. Y. Platelets in hemostasis and thrombosis: Novel mechanisms of fibrinogen-independent platelet aggregation and fibronectin-mediated protein wave of hemostasis. *J. Biomed. Res.* **2015**, *29*, 437–444.

[31] Kattula, S.; Byrnes, J. R.; Wolberg, A. S. Fibrinogen and fibrin in hemostasis and thrombosis. *Arterioscler. Thromb. Vasc. Biol.* **2017**, *37*, e13–e21.

[32] Gryshchuk, V.; Galagan, N. Silica nanoparticles effects on blood coagulation proteins and platelets. *Biochem. Res. Int.* **2016**, *2016*, 2959414.

[33] Wang, K.; Albert, K.; Mosser, G.; Haye, B.; Percot, A.; Paris, C.; Peccate, C.; Trichet, L.; Coradin, T. Self-assembly/condensation interplay in nano-to-microfibrillar silicified fibrin hydrogels. *Int. J. Biol. Macromol.* **2020**, *164*, 1422–1431.